



## Abstract

The deposition of fluvial sediments in tectonically active areas is mainly controlled by tectonics, climate, and associated Earth surface processes; consequently, fluvial sediments can provide a valuable record of changes in regional climate and tectonic activity. In this study, we conducted a detailed analysis of the grain-size distribution in modern fluvial sediments from the upper Min River, Eastern Tibet. These data, combined with information of regional climate, vegetation, hydrology, geomorphology, lithology, and fault slip rate, indicate that modern regional tectonic activity along upper Min River can be divided into three segments. Specifically, fluvial sediments in the segment I are dominated by silts ( $<63\ \mu\text{m}$ , 70.2%), agreeing with a low-runoff, low-rainfall and high vegetation cover and revealing a windblown origin influenced by the arid and windy climate. These observations are consistent with the low hillslope angle and low relief in segment I, all indicating weak activity along the Minjiang Fault. The coarse-grained fraction ( $>250\ \mu\text{m}$ ) of fluvial sediments in the segments II and III increases stepwise downstream, although runoff and rainfall do not change significantly from segment II to segment III. These patterns correlate well with increases in both regional relief and hillslope angles. Together, these observations imply that regional tectonic activity along Maoxian–Wenchuan Fault becomes more pervasive downstream along the Min River. The occurrence of well-sorted and well-rounded pebbles of fluvial sediments in downstream of Dujiangyan must be related to the long-time scouring and sorting by rivers. This study marks the first development of a new and important research approach that can characterize regional tectonic activity by analysis of grain-

36 size distribution of fluvial sediments collected from tectonically active regions.

37

38 **Keywords:** Modern fluvial sediments; Grain-size analysis; Tectonic activity; Upper

39 Min River; Eastern Tibetan Plateau

40

## 1 Introduction

Tectonic geomorphology is a relatively young sub-discipline of geomorphology, and has the major aim of unraveling interactions between tectonic activity, climate, and Earth surface processes (Wobus et al., 2005; Owen, 2013). The grain-size distribution of river bed material, channel width, channel sinuosity, extent of alluvial cover, lithology of bedrock, and hydraulic roughness are all potentially important variables (Whipple, 2004; Whittaker et al., 2010). Thus, comprehensive amounts of data must be collected in a wide range of field settings before the responses of these important variables to climatic and tectonic forcings can be determined.

The topographic margin of the Tibetan Plateau (TP) along the Longmen Shan is one of the most impressive continental escarpments in the world, and the land surface rises westward over a horizontal distance of 40–60 km from the Sichuan Basin (500–700 m elevation) to peak elevations exceeding 6000 m (Chen et al., 2000; Kirby et al., 2000, 2008). Some studies have revealed common topographic features within river channels in the eastern TP, namely, an upper low-gradient channel segment, a middle steep-gradient channel segment, and a low-lying very steep channel segment, such as in the Red River region in Yunnan Province (Schoenbohm et al., 2004) and the Min River region in Sichuan Province (Kirby et al., 2003). However, it is important to note that strong lithological contrasts along the length of a river can also cause the channel steepness index to change at comparable magnitudes to those associated with large gradients in rock uplift rate (Snyder et al. 2000; Stock and Dietrich 2003; Beek and Bishop 2003; Whittaker et al., 2010). New data sourced from several localities record an apparent narrowing of channel width in response to increased rock uplift rates in

64 rivers with large areas of bedrock (Whipple, 2004). This is consistent with the recent  
65 proposition that river profiles straighten as aridity increase (Chen et al., 2019), as  
66 observed along the upper Min River in the field. Generally, exposures of hard bedrock  
67 often generate straight channels, which have low channel slopes and small sediment  
68 loads (Schumm and Khan, 1971, 1972).

69 Vegetation density can modulate topographic responses to changing denudation  
70 rates, such that the functional relationship between denudation rate and topographic  
71 steepness becomes increasingly linear as vegetation density increases (Olen et al., 2016).  
72 Recent studies indicate that the upper Min River has poor vegetation coverage and most  
73 regions are fully exposed due to the strongly arid climate conditions (Jiang et al., 2015;  
74 Xu et al., 2020; Shi et al., 2020; Wei et al., 2021; Zhou et al., 2021). Thus, hillslope  
75 colluvium is the dominant sediment source to the upper Min River – especially in its  
76 middle and lower segments (Zhang et al., 2021) – akin to those in drainage basins in  
77 many arid regions worldwide (Clapp et al., 2002).

78 Tectonic activity influences the evolution of lacustrine sedimentary sequences by  
79 affecting the provenance supply (Najman, 2006; Jiang et al., 2022). Frequent  
80 earthquakes on the TP, as recorded by widely distributed soft sediment deformation  
81 (Wang et al., 2011; Xu et al., 2015; Jiang et al., 2016; Zhong et al., 2019; Zhang et al.,  
82 2021), caused repeated landslides that also represent another major source of sediment  
83 into the upper Min River (Dai et al., 2011; Xu et al., 2012, 2013). These landslides  
84 generated a large amount of dust storms that deposited dust in nearby lakes (Jiang et al.,  
85 2014, 2017) and exposed large quantities of fine-grained sediment that had  
86 accumulated on mountain slopes, which were subsequently transported by wind to  
87 ancient lakes, documenting these seismic events (Whittaker et al., 2010; Liang and  
88 Jiang, 2017; Shi et al., 2022). This sedimentological process was recently recognized at

Huojizhai, Diexi Town, following the historical earthquake at Diexi in 1933 (Wei et al., 2021).

Changes in hydrology and sediment flux are commonly regarded as climate forcing (Wobus et al., 2010). The extent of alluvial cover is very limited throughout the upper Min River Basin, which is demonstrated by similarity of zircon U–Pb ages in lacustrine sediments and their nearby bedrock units (Zhong et al., 2017). As such, the influence of occasional flood events should be considered over long time scales (Snyder and Whipple, 2003), as aridity precludes rainfall or fluvial undercutting as being the trigger for such events.

The consistent climate coupled with systematic variations in lithology and rock uplift rate along the Min Mountains allow comparison of channels that experience different tectonic forcings (Duvall et al., 2004). Selective transport is the dominant downstream fining mechanism in this region, although rates of selective transport in sand–bed rivers are smaller than those in gravel–bed rivers (Frings, 2008).

Only a small volume of sediment collected from a river bed is needed to produce a transformative understanding of the rates at which landscapes change (Blanckenburg, 2005). Study of these materials can reveal relationships between generation, transport (Clapp et al., 2000, 2002), and mixing of sediment (Perg et al., 2003; Nichols et al., 2005), under the help of the key topographic and/or lithologic features (e.g., relief, slope angle, and substrate characteristics) (Riebe et al., 2000; Riebe et al., 2001; Matmon et al., 2003a, b). In this study, we combine field surveys and analysis of river sediments in the upper Min River to determine hydraulic characteristics, and topographic and tectonic information about bedrock channels.

## **2 Regional setting**

## 2.1 Geographic and geologic settings

Instrumental data collected after 1900 indicate that the TP has experienced strong earthquakes clustered around the Bayan Kala Block from 1995 to the present day, which are collectively known as the Kunlun–Wenchuan earthquake series (Deng et al., 2014). The eastern TP is geomorphologically characterized by alpine valleys, and is tectonically controlled by the Longmen Shan thrust belts, the Minjiang Fault, and the Huya Fault (Fig. 1a). Frequent tectonic activities have led to numerous earthquakes and landslides in this region (e.g., Zhang et al., 2003; Jiang et al., 2014; Li et al., 2015; Liang and Jiang, 2017), such as the 1933 Diexi  $M_s$  7.5 earthquake, the 1976 Songpan  $M_s$  7.2 earthquake, the 2008 Wenchuan  $M_s$  8.0 earthquake and the 2017 Jiuzhaigou  $M_s$  7.0 earthquake. These earthquakes caused widespread damage to the Earth surface in this region. GPS–measured uplift rates in the Longmen Shan Fault zone reached 2–3 mm/a over 10 years since 1999 (Liang et al., 2013). Thermochronological dating of zircon and apatite indicated denudation rates of 1–2 mm/a in the Longmen Shan region during the Late Cenozoic (Kirby et al., 2002).

The alpine valleys in the eastern TP reduce the preservation potential of Quaternary sediments and expose large areas of bedrock. Bedrock outcrops within the catchment region of the upper Min River are dominated by Silurian phyllite, quartz schist, and Triassic phyllite, metamorphosed sandstone (Fig. 1a), which are easily weathered and eroded into transportable debris (Zhong et al., 2019). Massive granites are also exposed in the study area; in particular, the Neoproterozoic Pengguan complex (U–Pb age of 859–699 Ma; Ma et al., 1996) (Fig. 1a) is mainly composed of intermediate–acid intrusive rocks, with lesser amounts of basic–ultrabasic intrusive





al., 2014), nearly oriented N–S (Fig. 1b), and erodes the hinterland of the TP via formation of gullies and valleys. The Min River valley is typically steep, narrow and deepening downstream with an incision depth of 300–1500 m (e.g., Li et al., 2005; Zhang et al., 2005). The slopes on both sides of the study area are between 18° and 45°, and the vertical aspect ratio of the valley is 5.5–12.6 ‰ (Zhang et al., 2005). Constrained by the specific landforms of the alpine valleys, the wind direction in the study area is generally SSW/NNE, roughly consistent with the strike of local valleys (Liu, 2014). The Min River valley exhibits high wind speeds in April (average 4.9 m/s) and low speeds in July (average 3.7 m/s). Wind speed is generally < 4 m/s before noon and > 4 m/s after noon, and normally peaks approximately 8–10 m/s at around 16:00 (Liu, 2014). The highest instantaneous wind speed recorded in the study area was 21 m/s (Liu, 2014).

The upper reaches of the Min River are located in a transition zone on the TP where wet monsoonal climate changes to a high–elevation cold climate. In this region, mean annual precipitation (MAP) ranges from 400 mm to 850 mm, and precipitation is dominant (>75%) during the rainy season (May–October) (Ding et al., 2014). It is noticeable that orographic rain along the eastern TP generates two storm areas centered around Sandagu and Zipingpu (Fig. 1b). Statistical analyses of precipitation data from 1982 to 2007 show that the MAP within these regions is higher than 1200 mm (Ding et al., 2014).

Regional vegetation has clear vertical zonation, which mainly consists of small–leaf, arid shrubs at 1300–2200 m a.s.l., mixed broadleaf–conifer forests, evergreen and deciduous broad–leaved mixed forests at 2000–2800 m a.s.l., *Picea* and *Abies* forests at 2800–3600 m a.s.l., and alpine shrubs and meadows at > 3600 m a.s.l. (Ma et al., 2004; Zhang et al., 2008). There are two key factors that influence vegetation

distribution and ecological conditions in the study area: the arid and windy climate, which has a large temperature difference between day and night, and tectonics activity characterized by frequent earthquakes (Lin, 2008; Wang et al., 2011). For example, strong earthquakes often induce landslides that can destroy vegetation cover in the study area (Xu et al., 2012, 2014). Both of these factors lead to fragility in landscape and vegetation cover.

## 2.2 Segmented characteristics of the Min River

Based on the topographical and geomorphological characteristics, fault and vegetation distribution patterns, the upper Min River could be subdivided into four segments (Fig. 1b).

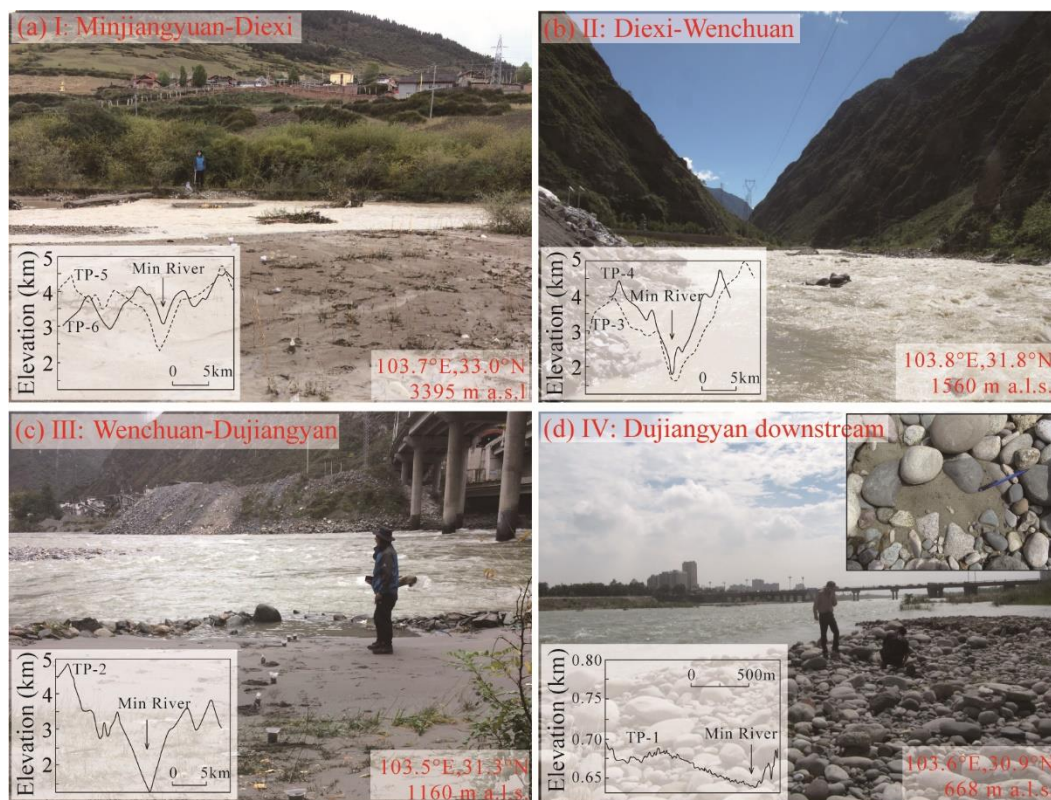


**Figure 2** Photographs of field sampling sites in the upper Min River. The locations of cross-sections through the Min River valleys (Zhang et al., 2005) are shown in Fig. 7c.

Segment I is the Minjiangyuan – Diexi segment (3460–2190 m a.s.l.). The riverbed

in this segment is directly connected with one side of the Min Mountain and has a valley bottom width of 200–1000 m (Zhang et al., 2005) (Fig. 2a). Downstream from Minjiangyuan, valley bottom width narrows markedly and is only 200–300 m in Zhenjiangguan – Diexi segment (Zhang et al., 2005). The relative relief of the Min Mountain increases significantly from Minjiangyuan to Diexi along the Min River, especially from Zhenjiangguan to Diexi (Zhang et al., 2005). The vegetation coverage along this segment gradually deteriorates, with *Picea*, *Abies*, shrubs, and herbs in the Minjiangyuan – Songpan segment, but only a small number of shrubs and herbs in the Songpan – Diexi segment. Bedrock is widely exposed in the lower part of the segment. In this region, the monthly maximum wind speed reaches 15.4 m/s in Songpan.

Segment II is the Diexi – Wenchuan segment (2190–1470 m a.s.l.). The valley bottom width in this segment decreases to 200–300 m (Zhang et al., 2005), and the Min Mountains always occur in direct contact with the riverbed of the Min River (Fig. 2b). The longitudinal slope (12.6‰) reaches its maximum regional value near Diexi (Zhang et al., 2005). The regional vegetation coverage is mostly sparse and the bedrock is well exposed.

Segment III is the Wenchuan–Dujiangyan segment (1470–900m a.s.l.). The valley bottom width in this segment widens to about 200–500 m (Zhang et al., 2005) (Fig. 2c) and regional vegetation cover increases compared to segment II. In particular, the hillside around the Zipingpu Reservoir is covered with thick broad-leaved trees and herbs. The monthly maximum wind speed in Lixian is 14.0 m/s.

Segment IV is the Dujiangyan – segment (900 – 630 m a.s.l.). This segment flows into the interior of the Sichuan Basin, where it has flat geomorphological features (i.e., the riverbed width is greater than 300 m; Fig. 2d), and then transitions into the middle reach of the Min River. The monthly maximum wind speed in Dujiangyan is 13.8 m/s.

### 3 Materials and methods

#### 3.1 Field sampling and grain-size analysis

A ~340 km transect along the upper Min River was conducted during October 2017, starting in the eastern TP (Minjiangyuan, 33°01'59"N, 103°42'42"E; 3462 m a.s.l.) and ending in the Sichuan Basin (Dujiangyan, 30°56'25"N, 103°38'14"E; 634 m a.s.l.) (Fig. 1b). A total of 181 river samples were collected for grain-size analysis at 25 sites (Table S1). Sampling sites were selected from exposed, freshly-developed depositional sequences that occurred close to the active channel and its margins (Fig. 2). Voluminous bedrock gravel occurs around the sampling sites (Fig. 2). To ensure sample consistency associated with uniform flow regimes, each sample was collected at a depth of 0–0.2 m from different places within each sampling sequence. All locations were carefully chosen to avoid contamination from riverbank materials or from anthropogenic reworking.

Grain-size analysis was conducted using a Malvern Mastersizer 3000 laser grain-size analyzer at the State Key Laboratory of Earthquake Dynamics, Institute of Geology, China Earthquake Administration in Beijing, China. About 0.5 g of sediment was pretreated with 20 ml of 30% H<sub>2</sub>O<sub>2</sub> to remove organic matter and then with 10 ml of 10% HCl to remove carbonates. About 300 ml of deionized water was added, and the sample solution was kept for 24 h to rinse acidic ions. The sample residue was dispersed with 10 ml of 0.05 M (NaPO<sub>3</sub>)<sub>6</sub> on an ultrasonic vibrator for 10 min before grain-size measurements. For each sample, the grain-size analyzer automatically outputs the

median diameter (Md) and the percentages of each size fraction, with a relative error of less than 1%. Magnetic susceptibility (SUS) was measured using a Bartington MS2 susceptibility meter.

### 3.2 Y values

Mean grain size (Ms), standard deviation ( $\sigma$ ), skewness (Sk), and kurtosis ( $K_G$ ) are commonly used to discriminate between different depositional processes and environments. Sahu (1964) distinguished aeolian processes from those that operate in a littoral environment by using the following equation:

$$Y = -3.5688 Ms + 3.7016 \sigma^2 - 2.0766 Sk + 3.1135 K_G \quad (1)$$

Here, Y values less than  $-2.74$  indicate an aeolian provenance and Y values greater than  $-2.74$  indicate a hydrogenic provenance (Sahu, 1964). Calculated Y values for lacustrine sediments (Jiang et al., 2017, 2014), red clay, and loess–paleosol deposits (Wu et al., 2017; Lu and An, 1999) are less than  $-2.74$ , indicating an aeolian provenance.

### 3.3 End–member analysis

Numerical unmixing of grain–size distribution data into constituent components, known as end–member analysis (EMA), can yield valuable information about transport dynamics (Weltje, 1997; Paterson and Heslop, 2015; Jiang et al., 2017). According to the principle that the end–member number (EM) should be as small as possible (Weltje et al., 1997), several EMs obtained by end–element analysis imply that numerous dynamic mechanisms occurred during formation of these deposits. Generally, larger values of EMs correspond to a stronger transport capacity, which itself indicates different provenances (Vandenberghe, 2013; Dietze et al., 2014; Jiang et al., 2017). For instance, the peak values of EMs in Lixian lacustrine sediments were concentrated at

10  $\mu\text{m}$  ( $\text{EM}_1$ ) and 40  $\mu\text{m}$  ( $\text{EM}_2$ ), and so reflect the background deposition of dust and locally sourced deposition transported by ambient wind, respectively (Jiang et al., 2017). We analyzed the Min River samples using the AnalySize software for processing and unmixing grain-size data (Paterson et al., 2015), with parameters selected from the generalized Gaussian skewness model (SGG) (Egli, 2003).

### 3.4 Analysis of C–M and F–M diagrams

The analysis of C–M and F–M diagrams is useful to interpret sediment transport dynamics (Passega, 1957; Singh et al., 2007). In these diagrams, C is the coarsest percentile of the grain-size distribution in samples (one percentile), and M is the median diameter of the grain-size distribution, which are both indicators of the maximum and average transport capacity, respectively (Passega, 1957; Singh et al., 2007; Bravard et al., 2014). In addition, F represents the percentage of fractions finer than 125  $\mu\text{m}$  (Singh et al., 2007). All values are plotted on a logarithmic scale, which produces specific patterns for distinct reaches (Singh et al., 2007; Bravard et al., 2014). A C–M diagram (Fig. S1) has the following sections: NO, rolling; OP, rolling with some grains transported in suspension; PQ, graded suspension with some grains transported by rolling; QR, graded suspension; RS, uniform suspension; and T, pelagic suspension (Passega, 1957; Bravard and Peiry, 1999; Bravard et al., 2014).

## 4 Results

### 4.1 Characteristics of grain-size and SUS

The median grain size ( $\text{Md}$ ), five grain-size fractions (0–2  $\mu\text{m}$ , 2–20  $\mu\text{m}$ , 20–63  $\mu\text{m}$ ,

63-250  $\mu\text{m}$ , >250  $\mu\text{m}$ ), SUS and Y values of the Min River sediment can be divided into four categories (Fig. 3), which correspond to the different segments (I – IV) defined above. The average values of Md increased significantly at Diexi (from 31.0  $\mu\text{m}$  to 80.8  $\mu\text{m}$ ) and Wenchuan (from 49.3  $\mu\text{m}$  to 170.2  $\mu\text{m}$ ), and decreased slightly at Dujiangyan (from 220.4  $\mu\text{m}$  to 119.2  $\mu\text{m}$ ). The variations at these three sites are the most significant within the whole river (Table 1, Fig. 3).

**Table 1** Statistics for grain-size fractions in the upper Min River.

Segments	Md ( $\mu\text{m}$ )	Percentage composition / (%)					SUS
		0–2	2–20	20–63	63–250	>250	
		$\mu\text{m}$	$\mu\text{m}$	$\mu\text{m}$	$\mu\text{m}$	$\mu\text{m}$	
I	31.0	2.8	40.3	27.1	23.7	6.2	11.6
II	80.8	0.4	25.3	20.3	34.6	19.4	11.3
III	170.2	0.3	20.0	13.9	31.9	33.8	193.5
IV	145.2	0.5	13.0	9.5	59.5	17.5	251.8

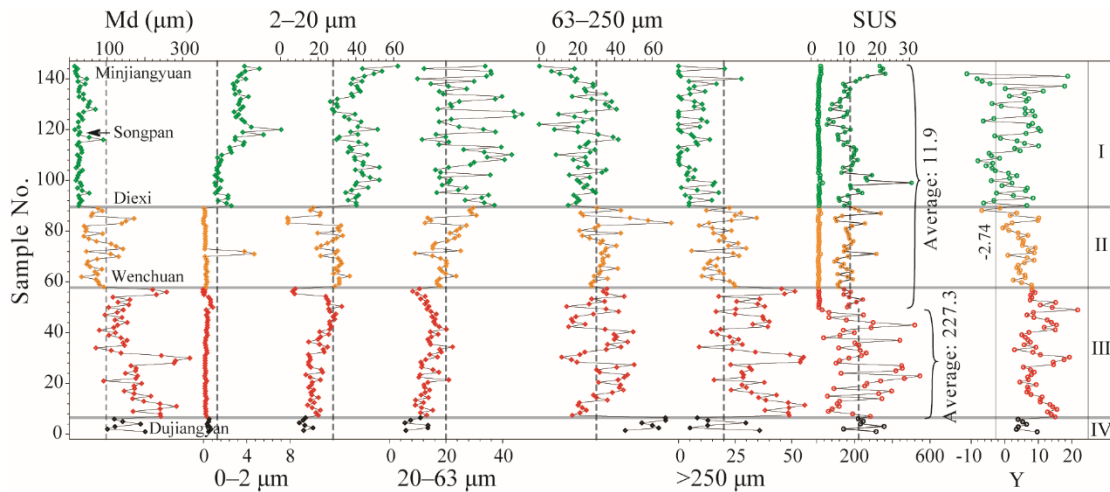


**Figure 3** Variation of grain-size components and river sediment parameters from the upper Min River. The dotted lines represent the average value of the whole sequence.

Along the upper Min River downwards, the mean proportion of the 2–20  $\mu\text{m}$  (I = 40.3%, II = 25.3%, III = 20.0%, and IV = 13.0%) and 20–63  $\mu\text{m}$  fractions (I = 27.1%,

II = 20.3%, III = 13.9%, and IV = 9.5%) exhibit a stepwise decrease (Table 1, Fig. 3). The 63–250  $\mu\text{m}$  fraction exhibits a sharp increase from segment I (23.7%) to II (34.6%) and from segment III (31.9%) to IV (59.5%), but a relatively minor change from segment II (34.6%) to III (31.9%) (Table 1, Fig. 3). The  $> 250 \mu\text{m}$  fractions exhibit a stepwise increase between segments I, II, and III (6.2%, 19.4%, and 33.8%, respectively), and a significant decrease from segment III (33.8%) to IV (17.5%) (Table 1, Fig. 3). Measured SUS values remained low in segments I (5.3–30.6, with a mean of 11.6) and II (7.1 to 21.2, with a mean of 11.3), but were significantly higher in segment III (9.9–546.5, with a mean of 193.5) and reached consistently high values in segment IV (142.1–356.5, mean: 251.8) (Table 1, Fig. 3).

#### 4.2 End-member analysis

Three end-members (EMs) ( $R^2 = 0.93$ ) were identified in the Min River samples (Fig. 4) with peaks of 21.2  $\mu\text{m}$  (58.0%), 185.8  $\mu\text{m}$  (24.2%), and 351.7  $\mu\text{m}$  (17.8%), respectively. Along the upper Min River downwards, these three EMs show clear stepwise changes between segments (Fig. 5). EM<sub>1</sub> shows a stepwise decrease (I = 82.5%, II = 53.1%, III = 38.6%, and IV = 23.7%), corresponding to the sum of the 2–20  $\mu\text{m}$  and 20–63  $\mu\text{m}$  fractions (Figs. 3, 5). EM<sub>2</sub> shows a sharp increase from segment I (13.1%) to II (31.4%) and from segment III (27.1%) to IV (67.4%), and a relatively smaller change from segment II (31.4%) to III (27.1%), corresponding to the 63–250  $\mu\text{m}$  fraction. By contrast, EM<sub>3</sub> corresponds to the  $>250 \mu\text{m}$  fraction (Figs. 3, 5) and shows a stepwise increase between segments I, II, and III (4.4%, 15.5% and 38.6%, respectively), and a significant decrease from segment III (38.6) to IV (23.7%).



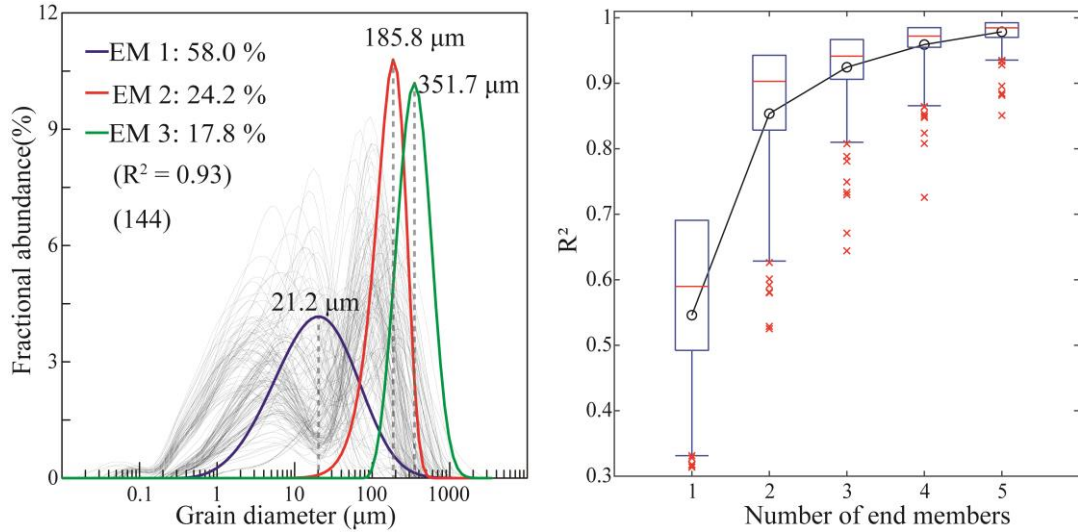


**Figure 4** End-member analysis model of fluvial sediments from the upper Min River.

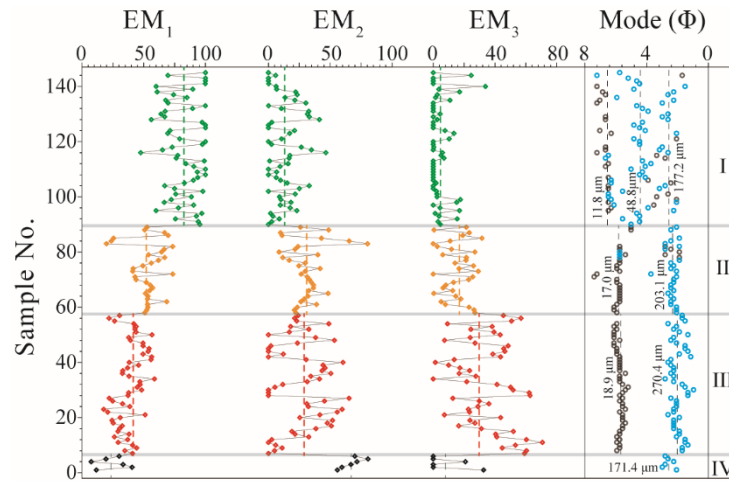


**Figure 5** Variability of EMs and mode values of samples collected from the upper Min River. The peak values (mode values) with  $>1\%$  fractional abundance of the grain-size frequency distributions were extracted after consideration of a  $1\%$  instrumental error. Blue and gray circles represent the main and secondary peak modal values, respectively. The dotted lines represent the average value.

### 4.3 Characteristics of the grain-size frequency distribution

The grain-size frequency of river samples from segment I has a discrete distribution (Fig. S2) with three mode values at  $\sim 11.8 \mu\text{m}$ ,  $\sim 48.8 \mu\text{m}$ , and  $\sim 177.2 \mu\text{m}$ . The main mode value of segment I occurred in the  $\sim 48.8 \mu\text{m}$  portion. The grain-size

frequency distribution for segments II and III is strongly bimodal (Fig. S2), with the major and minor mode values at  $\sim 203.1 \mu\text{m}$  and  $\sim 17.0 \mu\text{m}$  for segment II, and  $\sim 270.4 \mu\text{m}$  and  $\sim 18.9 \mu\text{m}$  for segment III. The grain-size frequency distribution for segment IV is unimodal (Fig. S2) with a mode value of  $\sim 171.4 \mu\text{m}$ .

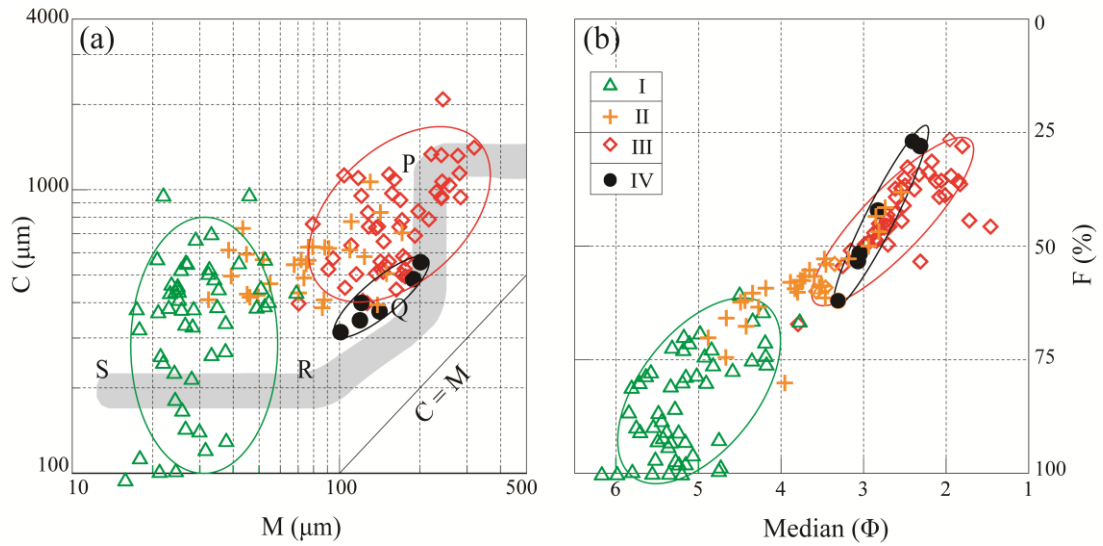


**Figure 6** C–M and F–M distributions of samples collected from the upper Min River.

#### 4.4 C–M and F–M diagrams

On a C–M diagram for the Min River, samples from segment I are completely separate from those collected from segments III and IV. Most samples in segment II overlap with those of segment III (Fig. 6a). Among them, the M value of segment I (13.9–89.8  $\mu\text{m}$ ) mainly belongs to the RS section (Fig. 6a), although the C values exhibit a large variation between 54.8  $\mu\text{m}$  and 964.3  $\mu\text{m}$ . Samples from segment II are distributed throughout the P–Q–R sections (Fig. 6a), have C values of 383.5–1066.0  $\mu\text{m}$ , and M values of 32.2–171.4  $\mu\text{m}$ . Samples from segment III are concentrated in the PQ section (Fig. 6a), have C values of 396.9–2083.8  $\mu\text{m}$ , and M values of 70.3–319.1

μm. Samples in segment IV plot close to the RQ section and are distributed parallel to the C = M line (Fig. 6a). Samples collected from segments of the Min River show similar distribution features in F–M diagrams to those shown in C–M diagrams (Fig. 6).

## 5 Discussion

### 5.1 Dynamic and provenance implications of fluvial sediments

Grain-size fractions, EMs, and mode values in different segments along the upper reaches of Min River reflect the distinct provenance and transport dynamics of fluvial sediments (McKinney and Sanders, 1978; Sun et al., 2002, 2004; Sun et al., 2007; Dietze et al., 2014; Vandenberghe, 2013). The EM<sub>1</sub> in segment I reaches a proportion of 82.5%, which corresponds to the fine particle components (<63 μm fractions). Previous studies have indicated that fractions with sizes of <10 μm and 10–40 μm represent background particles and regional dust that have been transported by wind (Dietze et al., 2014; Jiang et al., 2014, 2017), which contribute 51±11% and 42±14% of the lacustrine sediments across the TP, respectively (Dietze et al., 2014). Therefore, the EM<sub>1</sub> (fine-grained fractions) in segment I probably have an aeolian provenance. This inference is supported by five separate lines of evidence: 1) Md varies within the narrow range 13.9–89.8 μm (Fig. 3), although the C values fluctuate widely between 54.8 μm and 964.3 μm (Fig. 7); 2) the distribution of samples in an RS section in a C–M diagram (Fig. 6) reflects uniform suspension, which likely requires transportation by ubiquitous and strong wind (Fig. S1, Passega, 1957); 3) nearly half of the samples (i.e.,

22 out of 55) have Y values of less than  $-2.74$ , which is indicative of an aeolian origin (Sahu, 1964); 4) loess deposits are widely distributed in the study area, especially from Diexi upstream (Fig. S3) (Liu et al., 2013; Shen et al., 2017) and may represent a voluminous source of dust particles; and 5) the study area has a high mean altitude of 2840 m, and the monthly maximum wind speed can reach 15.4 m/s, which would allow for strong aeolian transport.

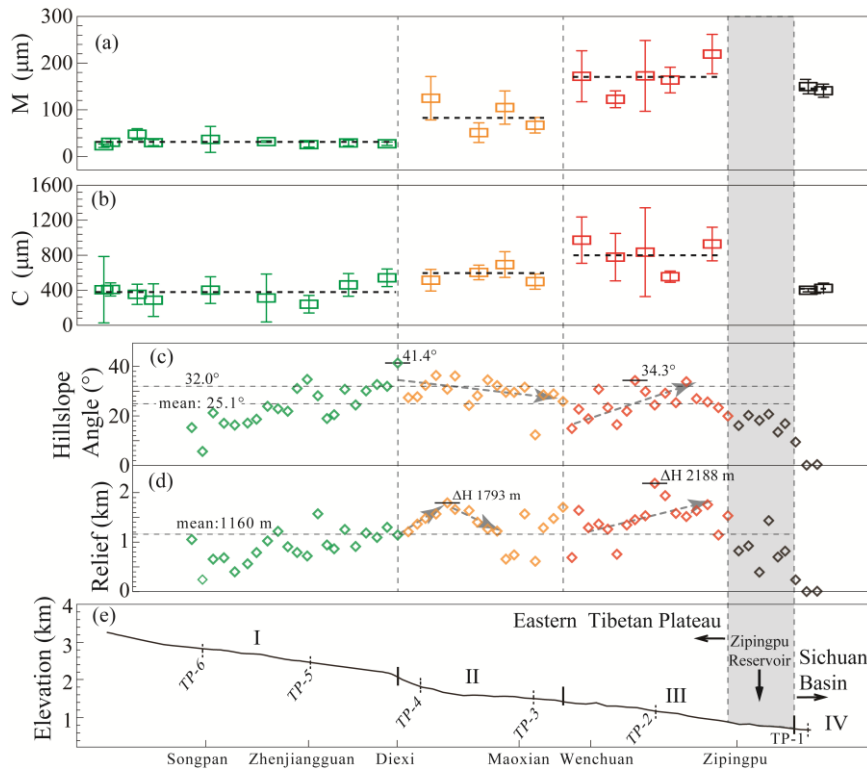


**Figure7** Variation characteristics of (a) M and (b) C values of the grain-size index. (c) Riverbed base-level and the position of the cross-section of the upper Min River (Zhang et al., 2005). (d) Hillslope angle and (e) local relief along the upper Min River. A 4\*4 km grid was delineated along the upper Min River (~260 km). The highest ridgeline and riverbed height in the grid were extracted from a DEM map, and the local relief was then obtained by calculating the highest ridgeline minus the riverbed height.

The hillslope angle was obtained by solving for  $\tan$  (local relief/slope length).

The EM<sub>2</sub> in segment IV reaches the highest value (185.8  $\mu\text{m}$ : 67.4%) recorded in the whole sequence and corresponds to the 63–250  $\mu\text{m}$  fraction (59.5%), which is consistent with previous studies having shown that fluvial deposits are composed mainly of a medium–sand component (modal size: 200–400  $\mu\text{m}$ ) (Middleton, 1976; Tsoar and Pye, 1987; Bennett and Best, 1995; Dietze et al., 2014). In the C–M diagram, sample data that lie close to the  $C = M$  line reflect the suspension transport of riverbed sediments (Fig. 6a) (Singh et al., 2007; Passega, 1957). In addition, the single peak mode (Fig. S2d) of segment IV represents a single river transport process and sedimentary environment (McKinney and Sanders, 1978), and the small size range of the grain–size frequency distribution also reflects a well–sorted product that was deposited by fluvial action (Sun et al., 2002). Therefore, the EM<sub>2</sub> mainly reflect typical fluvial sediments.

EM<sub>3</sub> corresponds to the coarsest grain–size components (>250  $\mu\text{m}$ ) and has the highest value (351.7  $\mu\text{m}$ : 38.6%) of the whole sequence in segment III. The maximum values of C and M (Figs. 7a, b) in segment III indicate that it had the highest transport capacity (Passega, 1957; Singh et al., 2007; Bravard et al., 2014). Therefore, EM<sub>3</sub> represents the local sedimentary component that was locally transported over short distances (Dietze et al., 2014; Jiang et al., 2014, 2017). The distribution characteristics of samples from segment III in the PQ section (Fig. 6a) indicate that dominant rolling and jumping transportation processes (Passega, 1957). Meanwhile, the SUS values in segment III increase to abnormally high values (28.5–546.5, with a mean of 227.3)

abruptly near to exposures of the Pengguan complex (Fig. 1a), although lower SUS values occur in the surrounding area (Zagunao River: 9.1–114.1, with a mean of 34.1, Fig. S4; Zipingpu reservoir: 5–60, Zhang et al., 2019; and segments I and II: 5.3–30.6, mean 11.5, Fig. 3). The precipitation in segment III is generally low (400–700 mm/a) and only significantly increases near to the Zipingpu reservoir (1200 mm/a), so that the sedimentary changes were muted until 2 years after the Wenchuan earthquake (Zhang et al., 2019) (Fig. 1b). In addition, the mean grain size in segment III (170.2  $\mu\text{m}$ ) increases before the Zagunao River (mean of 83.1  $\mu\text{m}$ , Fig. S4) joins the Min River (Fig. 1b. 3) and contribution from the Zagunao River can be precluded. Therefore, the abnormally high grain size and SUS values in segment III are likely caused by a local provenance change.

## **5.2 Climate controlled fine-grained fluvial sediments**

The windy and semi-arid climate in the study area is responsible for more fine particle components ( $\text{EM}_1$ ) in segment I (Jiang et al., 2014), which caused  $\text{EM}_1$  to gradually decrease downstream as the wind weakens (Fig. 5). The relatively low precipitation (400–700 mm/a) and low runoff ( $18.4\text{--}43.4 \times 10^8 \text{ m}^3$ ) (Fig. 1b) in segment I reflect the limited transport capacity of the river, and the angular gravels on the riverbed also indicate weak scouring, which preserves more fine-grained components ( $\text{EM}_1$ ) in fluvial sediments. Segment I developed along the Minjiang Fault (Fig. 1a), which has a low slip rate (0.30–0.53 mm/a, Kirby et al., 2000; Zhou et al., 2000, 2006; Tan et al., 2019) and therefore a weak influence on local provenance supply (Jiang et al., 2014, 2017). In addition, the wide riverbed (Fig. 2a), relatively low hillslope angle,

and local relief in the Minjiangyuan – Songpan segment (Figs. 7d, e) causes *in situ* retention of locally sourced coarse components. Therefore, EM<sub>2</sub> and EM<sub>3</sub> make only a minor contribution to the fluvial sediments in segment I.

Segment IV is located inside the Sichuan Basin and is completely unaffected by alpine valleys in the eastern TP. It is characterized by a wide and flat geomorphological surface (Fig. 2d). The significant downstream increase in precipitation and runoff in the Zipingpu reservoir (Fig. 1b) indicates that fluvial action was the main control on sediment transportation in segment IV. In addition, well-rounded pebbles (Fig. 2d) on the riverbed prove this point.

### **5.3 Coarse-grained deposits controlled by tectonism**

Fluvial sediments coarsen at the transition between segments I and II, highlighting an increase in EM<sub>2</sub> and EM<sub>3</sub> content, and a higher M value (Figs. 3, 7). This locality occurs at intersection of the Minjiang Fault and the Songpinggou Fault (Fig. 1a), which was the epicenter of the Diexi *Ms* 7.5 earthquake in 1933 (Chen et al., 1994; Ren et al., 2018). As a result, the outcropping bedrock was severely damaged and so provided new, fresh, and local sediment sources (EM<sub>3</sub>). Downstream from Diexi, field surveys exhibit that the altitude decreases by 400 m over a horizontal distance of 20 km, such that the longitudinal slope of the riverbed (12.6‰, Fig. 7c, Zhang et al., 2005) and the hillslope angle (41.4°, Fig. 7d) are highest in this region when compared to the entire study area, which imply a higher regional denudation rate forced by active tectonics (Zhang et al., 2005; Whittaker et al., 2007a). These remarkable changes of geomorphology correspond well to a twofold increase in erosion coefficients that occur within 15 km of major faults in the eastern TP (Kirkpatrick et al., 2020) and more intense denudation at the location of seismogenic faulting along high-relief plateau margins (Li et al.,

2017). The narrower valley and direct contact between the riverbed and hillside on either side in segment II (Fig. 2b) provide favorable conditions for rolling and jumping transportation of sediment along the hillslope. In addition, the rapid rising of the base-level of the Min River in segment II enhances the river's cutting and transport capacity (Merritts and Vincent, 1989; Stokes et al., 2002; Cheng et al., 2004; Whittaker et al., 2007a; Boulton et al., 2014).

EM<sub>3</sub> rapidly reaches its maximum fluctuation range in segment III (Fig. 5), likely due to the maximum transport force (C value) in the area (Fig. 7). The regional precipitation in segment III is low (400–700 mm/a) and only significantly increases near to the Zipingpu reservoir (1200 mm/a) (Fig. 1b). From a tectonic perspective, the Maoxian–Wenchuan Fault, with a large dextral slip rate (1.0–3.8mm /a; Chen and Li, 2013; Wang et al., 2017) and a large vertical slip rate (~1–2 mm/a; Liu et al., 2015), mainly controls the distribution of segment III (Fig.1). Previous studies have shown that the Maoxian – Wenchuan Fault occurs a band of maximum exhumation along the eastern Longmen Shan Fault zone since the late Miocene (Tan et al., 2019). Therefore, rapid regional uplift and denudation (Kirby et al., 2002; Liang et al., 2013) not only generated a larger hillslope angle (mean value of 24.9°) and the highest local relief (2188 m), but also provided widespread source of fresh, coarse-grained, and local sediment (Whittaker et al., 2007b, 2010) in segment III. The significant coarsening of fluvial sediment at the beginning of segment III indicates the catchments undergoing a transient response to tectonics are associated with significant volumetric export of material (Whittaker et al., 2010). Moreover, the PQ distribution of segment III samples in the calculated C–M diagram (Fig. 4) shows the importance of rolling and jumping



transport mechanisms (Passegga, 1957), which correlate with the steep landform features in segment III (Fig. 2c). Exposures of hard Mesozoic granites instantaneously provide a local source of coarse components, and thus correspond to the maximum M and C values. Although regional climate generally has a weak influence on the supply of coarse particles, the concentrated distribution of particles within the calculated grain-size frequency distribution (Fig. S2c) indicates that fluvial action played an effective role in sorting local sediment sources (Sahu, 1964; Sun et al., 2002; Frings, 2008). The persistent occurrence of the coarsest grain-size cross the segment III responds to the fact that the catchments crossing faults maintain their high slip rate over time, which exhibits a sharp contrast to that of segment I.

Generally, a large earthquake is followed by a period of enhanced mass wasting and fluvial sediment evacuation (Hovius et al., 2011; Wang et al., 2015). The Wenchuan *M*<sub>s</sub> 8.0 earthquake in 2008 caused severe geomorphological damage in region, and the annual average suspended sediment flow in regional rivers increased by a factor of 3–7 following the earthquake. The river recovered to its pre-earthquake level just  $1.2 \pm 0.9$  years later (Wang et al., 2015). However, over 70% of the co-seismic debris has stabilized in place along the hillslopes during the following decades (Dai et al., 2021) and will take 370 years to be removed out of the mountains (Wang et al., 2017). As such, we believe that co-seismic debris generated by the Wenchuan earthquake in 2008 had negligible influence on our sample collection campaign conducted in 2017.

#### **5.4 Geomorphic morphology reveals tectonic activity**

Alpine valleys characterize the landscape of the upper reaches of the Min River in

the eastern TP (Figs. 2, 7) and have an incision depth of 300–1500 m (Li et al., 2005; Zhang et al., 2005) (Fig. 6a). In segment I, hillslope angles and local relief gradually increase downstream along the Minjiang Fault from 5° to 34.8° and 243 m to 1572 m, respectively (Fig. 7d, e). However, these changes seem to be decoupled with the high and stable proportion of fine-grained background dust in the fluvial sediments of segment I (Figs. 3, 5), which is an open and interesting question. The consistent precipitation and runoff rates explain the calculated consistency in transport power, as defined by unchanging values of C and M (Fig. 7). We note that the longitudinal slope of the riverbed (6.7–7.6‰, Fig. 7c; Zhang et al., 2005) in segment I steadily changes as altitude decreases from 3460 m to 2190 m; therefore, gradual steepening of the landscape is likely a response to enhanced river-related erosion (Merritts and Vincent, 1989; Stokes et al., 2002; Cheng et al., 2004). The high vegetation density in the Minjiangyuan – Songpan region is also probably modulated by the lower topographic slope (Figs. 2a, 7) (Olen et al., 2016). These are consistent with generally weak activity of the Minjiang Fault (Kirby et al., 2000; Zhou et al., 2000, 2006; Tan et al., 2019).

In segment II, the hillslope angle (12.3–41.4°, with a mean of 30.1°) is generally steeper than the average for the whole study area (25.1°), and the highest angles (41.4°) far exceed the stability threshold of ~32° for landslide denudation, which suggests that landslide-dominated hillslope denudation has kept pace with the rates of rock uplift and valley incision in segment II (Burbank, et al., 1996; Montgomery and Brandon, 2002; Clarke and Burbank, 2010; Wang et al., 2014). Along the studied transect, local relief in segment II initially increases and then decreases (Fig. 7c), and the flow direction of

the Min River also changes from roughly N–S to NW–SE (Fig. 1a). The lithology in segment II changes from Triassic to Silurian (Fig. 1a), and seismic activity transitions from the Minjiang Fault to the Maoxian – Wenchuan Fault. Given that segment II records the lowest annual rainfall in the study area ( $<500$  mm/a, Fig. 1), this transformation of tectonic activity and lithology likely plays a dominant role on fluvial erodibility (Selby, 1980; Stokes et al., 2008; Whittaker et al., 2007a; Zondervan et al., 2020), and influences changes of regional geomorphology and river drainage.

Hillslope angles ( $14.9^{\circ}$ – $34.3^{\circ}$ , with a mean of  $24.9^{\circ}$ ) and local relief (689–2188 m, with a mean of 1463 m) in segment III exhibit a general increase along the Maoxian – Wenchuan Fault (Figs. 1, 7), although they differ from the increasing trends shown in segment I. For example, the highest local relief throughout the entire sequence occurs in segment III, although its mean hillslope angle ( $24.9^{\circ}$ ) is lower than the mean value ( $25.1^{\circ}$ ) of the entire sequence (Fig. 7). In addition, precipitation and runoff only show a significant increase adjacent to the Zipingpu reservoir (Fig. 1). We note that the regional bedrock in segment III is dominated by hard Mesozoic granites of the Pengguan complex (Fig. 1a), and that the Maoxian–Wenchuan Fault is situated on the zone of maximum exhumation along the Longmen Shan fault zone (Tan et al., 2019). Therefore, the higher local relief along segment III indicates that active Maoxian–Wenchuan Fault (Tan et al., 2019) caused enhanced rock uplift and valley incision (Whittaker et al., 2007a; Tan et al., 2019), which accounts for the largest transport forces (C values, Fig. 7) and the coarsest local components (EM<sub>3</sub>, Fig. 5) in this section. Nevertheless, a decrease in the mean hillslope angle within segment III may be

attributed to hardening of the exposed bedrock of the Pengguan complex rather than weakening of tectonic activity along the Maoxian–Wenchuan Fault. Even if the shortening rates are generally slow in the eastern TP (Densmore et al., 2008; Zhang, 2013) and satellite data may be equivocal, grain-size analysis of fluvial sediments combined with topographic analyses can help guide the identification of regional tectonic activity effectively (Schoenbohm et al., 2004; Kirby et al., 2003, 2008; Tan et al., 2019).

## **6 Conclusion**

Grain-size analysis was conducted on modern fluvial sediments of the upper Min River and this information was integrated with vegetation, hydrology, geomorphology (local relief and hillslope) and geology (fault and lithology) data to extract regional climate and tectonic signals in the eastern TP. This procedure identified three segments of tectonic activity along the upper Min River. The Minjiang Fault, situated in the Minjiangyuan – Diexi segment, generally shows weak tectonic activity. The Maoxian–Wenchuan Fault from Diexi to Wenchuan and from Wenchuan to Dujiangyan show enhanced phase of regional tectonic activity. However, the segment from Dujiangyan to the Sichuan basin records almost no evidence of tectonic activity.

In this study, we report a new approach that can reveal the style of regional tectonic activity by analyzing fluvial sediments collected from tectonically active regions. The novelty of this research method and the reliability of the results in this study provide a key framework with which regional tectonic activity can be revealed through the study

of fluvial sediments in other tectonically active localities worldwide.

#### **Data availability**

Data are available in the figshare database (<https://doi.pangaea.de/10.6084/m9.figshare.17111402>).

#### **Author contributions**

The paper was written by WS and HCJ with major contributions by HYX. SYM got geomorphic data. WS, HYX and SQZ participated in field surveys and sample collection. SQZ, JWF and XTW conducted laboratory tests and interpreted the results. All authors reviewed and approved the paper.

#### **Competing interests**

The contact author has declared that neither they nor their co-authors have any competing interests.

#### **Acknowledgements**

This study was supported by the National Nonprofit Fundamental Research Grant of China, Institute of Geology, China Earthquake Administration (IGCEA2126 and IGCEA1906).

#### **References**

- Beek, V.D., Bishop, P.: Cenozoic river profile development in the upper Lachlan catchment (SE Australia) as a test of quantitative fluvial incision models. *J. Geophys. Res. Solid Earth*, 108(B6), 2309, <https://doi.org/10.1029/2002JB002125>, 2003.
- Bennett, S.J., Best, J.L.: Mean flow and turbulence structure over fixed, two-dimensional dunes: implications for sediment transport and bedform stability. *Sedimentology*, 42(3), 491-513, <https://doi.org/10.1111/j.1365-3091.1995.tb00386.x>, 1995.
- Blanckenburg, F.: The control mechanisms of erosion and weathering at basin scale from cosmogenic nuclides in river sediment. *Earth Planet. Sci. Lett.*, 237, 462-479, <https://doi.org/10.1016/j.epsl.2005.06.030>, 2005.
- Boulton, S.J., Stokes, M., Mather, A.E.: Transient fluvial incision as an indicator of active faulting and Plio-Quaternary uplift of the Moroccan High Atlas. *Tectonophysics*, 633(1), 16-33, <https://doi.org/10.1016/j.tecto.2014.06.032>, 2014.
- Bravard, J.P., Goichot, M., Tronchère, H.: An assessment of sediment-transport processes in the Lower Mekong River based on deposit grain sizes, the CM technique and flow-energy data. *Geomorphology*, 207, 174-189, <https://doi.org/10.1016/j.geomorph.2013.11.004>, 2014.
- Burbank, D. W., Blythe, A. E., Putkonen, J., Pratt-Sitaula, B., Gabet, E., Oskin, M., Barros, A., Ojha, T. P.: Decoupling of erosion and precipitation in the Himalayas. *Nature*, 426(6967), 652-655, <https://doi.org/doi:10.1038/nature02187>, 2003.
- Burbank, D.W., Fielding, E., Anderson, R.S., Brozovic, N., Reid, M. D.C., Leland, J.: Bedrock incision, rock uplift and threshold hillslopes in the northwestern Himalayas. *Nature*, 379(6565), 505-510, <https://doi.org/10.1038/379505a0>, 1996.
- Chen, H., Li, Y.: Water system responding to the dextral strike-slipping of the Longmen Shan fault zone in the upper Min River basin. *J. Mount. Sci.*, 31(2), 211-217, <https://doi.org/10.3969/j.issn.1008-2786.2013.02.010>, 2013 (in Chinese).
- Chen, S.A., Michaelides, K., Grieve, S.W.D., Singer, M.B.: Aridity is expressed in river topography globally. *Nature*, 573, 573-577, <https://doi.org/10.1038/s41586-019-1558-8>, 2019.
- Chen, S.F., Wilson, C., Deng, Q.D., Zhao, X.L. Zhi, L.L.: Active faulting and block movement associated with large earthquakes in the Min Shan and Longmen Mountains, northeastern Tibetan Plateau. *J. Geophys. Res. Solid Earth*, 99(B12), 24025-24038,

<https://doi.org/10.1029/94JB02132>, 1994.

Chen, Z., Burchfiel, B.C., Liu, Y., King, R.W., Royden, L.H., Tang, W., Wang, E., Zhao, J., Zhang, X.: Global positioning system measurements from eastern Tibet and their implications for India/Eurasia intercontinental deformation. *J. Geophys. Res. Solid Earth*, 105(B7), 16215-16227, <https://doi.org/10.1029/2000jb900092>, 2000.

Cheng, S.P., Deng, Q.D., Li, C.Y., Yang, G.Z.: Dynamical mechanism, physical erosion processes and influence factors of fluvial incision: A review and prospect. *Quat. Sci.*, 24, 421-429, <https://doi.org/10.3321/j.issn:1001-7410.2004.04.008>, 2004 (in Chinese).

Clapp, E.M., Bierman, P.R., Caffee, M.: Using  $^{10}\text{Be}$  and  $^{26}\text{Al}$  to determine sediment generation rates and identify sediment source areas in an arid region drainage basin. *Geomorphology*, 45, 89-104, [https://doi.org/10.1016/S0169-555X\(01\)00191-X](https://doi.org/10.1016/S0169-555X(01)00191-X), 2002.

Clapp, E.M., Bierman, P.R., Schick, A.P., Lekach, J., Enzel, Y., Caffee, M.: Sediment yield exceeds sediment production in arid region drainage basins, *Geology*, 28, 995-998, [https://doi.org/10.1130/0091-7613\(2000\)28<995:SYESPI>2.0.CO;2](https://doi.org/10.1130/0091-7613(2000)28<995:SYESPI>2.0.CO;2), 2000.

Clarke, B.A., Burbank, D.W.: Bedrock fracturing, threshold hillslopes, and limits to the magnitude of bedrock landslides. *Earth Planet. Sci. Lett.*, 297(3-4), 577-586, <https://doi.org/10.1016/j.epsl.2010.07.011>, 2010.

Dai, F.C., Xu, C., Yao, X., Xu, L., Tu, X.B., Gong, Q.M.: Spatial distribution of landslides triggered by the 2008 Ms 8.0 Wenchuan earthquake, China. *J. Asian Earth Sci.*, 40, 883-895, <https://doi.org/10.1016/j.jseae.2010.04.010>, 2011.

Dai, L.X., Scaringi, G., Fan, X.M., Yunus, A.P., Liu, Z.J., Xu, Q., Huang, R.Q.: Coseismic debris remains in the orogen despite a decade of enhanced landsliding. *Geophys. Res. Lett.*, <https://doi.org/10.1029/2021GL095850>, 2021.

Deng, Q.D., Cheng, S.P., Ma, J., Du, P.: Seismic activities and earthquake potential in the Tibetan Plateau. *Chinese J. Geophys.*, 57(5), 2025-2042, <https://doi.org/10.1002/cjg2.20133>, 2014 (in Chinese).

Densmore, A. L., Ellis, M.A., Yong, L., Zhou, R., Richardson, N.: Active tectonics of the Beichuan and Pengguan faults at the eastern margin of the Tibetan Plateau. *Tectonics*, 26(4), TC4005, <https://doi.org/10.1029/2006TC001987>, 2008.

Duvall, A., Kirby, E., Burbank, D.: Tectonic and lithologic controls on bedrock channel profiles and processes in coastal California. *J. Geophys. Res. Earth Surface*, 109, F03002,

638 <https://doi.org/10.1029/2003JF000086>, 2004.

639 Dietze, E., Maussion, F., Ahlborn, M., Diekmann, B., Hartmann, K., Henkel, K., Kasper, T., Lockot,  
640 G., Opitz, S., Haberzettl, T.: Sediment transport processes across the Tibetan Plateau inferred  
641 from robust grain-size end members in lake sediments. *Clim. Past*, 10, 91-106,  
642 <https://doi.org/10.5194/cp-10-91-2014>, 2014.

643 Ding, H.R., Ma, G.W., Ni, S.J., Shi, Z.M., Zhao, G.H., Yan, L., Yan, Z.K.: Study on sediment  
644 discharge increase caused by Wenchuan earthquake landslide and heavy rainfall in the upper  
645 reaches of the Min River. *J. Sichuan Univ.*, 46(3), 49-55,  
646 <https://doi.org/10.15961/j.jsuese.2014.03.006>, 2014 (in Chinese).

647 Egli, R.: Analysis of the field dependence of remanent magnetization curves. *J. Geophys. Res. Solid*  
648 *Earth*, 108(B2), 1-26, <https://doi.org/10.1029/2002JB002023>, 2003.

649 Frings, R.M.: Downstream fining in large sand-bed rivers. *Earth Sci. Rev.*, 87, 39-60,  
650 <https://doi.org/10.1016/j.earscirev.2007.10.001>, 2008.

651 Hovius, N., Meunier, P., Lin, C.W., Chen, H., Chen, Y.G., Dadson, S., Horng, M.J., Lines, M.:  
652 Prolonged seismically induced erosion and the mass balance of a large earthquake. *Earth Planet.*  
653 *Sci. Lett.*, 304(3-4), 347-355, <https://doi.org/10.1016/j.epsl.2011.02.005>, 2011.

654 Jiang, H., Zhang, J., Zhang, S., Zhong, N., Wan, S., Alsop, G.I., Xu, H., Guo, Q., Yan, Z.: Tectonic  
655 and climatic impacts on environmental evolution in East Asia during the Palaeogene. *Geophys.*  
656 *Res. Lett.*, 49, e2021GL096832, <https://doi.org/10.1029/2021GL096832>, 2022.

657 Jiang, H.C., Shevenell, A., Yu, S., Xu, H.Y., Mao, X.: Decadal- to centennial-scale East Asian  
658 summer monsoon variability during the Medieval Climate Anomaly reconstructed from an  
659 eastern Tibet lacustrine sequence. *J. Paleolimnology*, 54, 205-222,  
660 <https://doi.org/10.1007/s10933-015-9847-1>, 2015.

661 Jiang, H.C., Mao, X., Xu, H.Y., Yang, H.L., Ma, X.L., Zhong, N., Li, Y.H.: Provenance and  
662 earthquake signature of the last deglacial Xinmocun lacustrine sediments at Diexi, East Tibet.  
663 *Geomorphology*, 204, 518-531, <https://doi.org/10.1016/j.geomorph.2013.08.032>, 2014.

664 Jiang, H.C., Zhong, N., Li, Y.H., Ma, X.L., Xu, H.Y., Shi, W., Zhang, S.Q., Nie, G.Z.: A continuous  
665 13.3-ka record of seismogenic dust events in lacustrine sediments in the eastern Tibetan Plateau.  
666 *Sci. Rep.*, 7:15686, <https://doi.org/10.1038/s41598-017-16027-8>, 2017.

667 Jiang, H.C., Zhong, N., Li, Y.H., Xu, H.Y., Yang, H.L., Peng, X.P.: Soft sediment deformation  
668 structures in the Lixian lacustrine sediments, Eastern Tibetan Plateau and implications for



669 postglacial seismic activity. *Sediment. Geol.*, 344, 123-134,  
 670 <https://doi.org/10.1016/j.sedgeo.2016.06.011>, 2016.

671 Kirby, E., Whipple, K.X., Burchfiel, B.C., Tang, W.Q., Berger, G., Sun, Z.M., Chen, Z.L.:  
 672 Neotectonics of the Min Shan, China: implications for mechanisms driving quaternary  
 673 deformation along the eastern margin of the Tibetan Plateau. *GSA Bull.*, 112(3), 375-393,  
 674 [https://doi.org/10.1130/0016-7606\(2000\)112<375:NOTMSC>2.0.CO;2](https://doi.org/10.1130/0016-7606(2000)112<375:NOTMSC>2.0.CO;2), 2000.

675 Kirby, E., Reiners, P.W., Krol, M.A., Whipple, K.X., Hodges, K.V., Farley, K.A., Tang, W.Q., Chen,  
 676 Z.L.: Late Cenozoic evolution of the eastern margin of the Tibetan Plateau: inferences from  
 677  $^{40}\text{Ar}/^{39}\text{Ar}$  and, U-Th/He thermochronology. *Tectonics*, 21(1), 1-20,  
 678 <https://doi.org/10.1029/2000TC001246>, 2002.

679 Kirby, E., Whipple, K. and Harkins, N.: Topography reveals seismic hazard. *Nat. Geosci.*, 1(8), 485-  
 680 487, <https://doi.org/10.1038/ngeo265>, 2008.

681 Kirby, E., Whipple, K.X., Tang, W.Q. and Chen, Z.L.: Distribution of active rock uplift along the  
 682 eastern margin of the Tibetan Plateau: Inferences from bedrock channel longitudinal profiles.  
 683 *J. Geophys. Res. Solid Earth*, 108(B4), 2217, <https://doi.org/doi:10.1029/2001JB000861>, 2003.

684 Kirkpatrick, H.M., Moon, S., Yin, A., Harrison, T.M.: Impact of fault damage on eastern Tibet  
 685 topography. *Geology*, 48, <https://doi.org/10.1130/G48179.1>, 2020.

686 Li, G., Westa, A.J., Densmoreb, A.L., Jin, Z.D., Zhang, F., Wang, J., Clark, M., Hilton, R.G.:  
 687 Earthquakes drive focused denudation along a tectonically active mountain front. *Earth Planet.*  
 688 *Sci. Lett.*, 472, 253-265, <https://doi.org/10.1016/j.epsl.2017.04.040>, 2017.

689 Li, Y., Cao, S.Y., Zhou, R.J., Densmore, A.L., Ellis, M.: Late Cenozoic Minjiang incision rate and  
 690 its constraint on the uplift of the eastern margin of the Tibetan plateau. *Acta Geol. Sinica*, 79(1),  
 691 28-37, <https://doi.org/10.3321/j.issn:0001-5717.2005.01.004>, 2005 (in Chinese).

692 Li, Y.H., Jiang, H.C., Xu, H.Y., Liang, L.J.: Analyses on the triggering factors of large quantities of  
 693 landslides in the upper reaches of the Minjiang River, Sichuan province. *Seism. Geol.*, 37(4),  
 694 1147-1161, <https://doi.org/10.3969/j.issn.0253-4967.2015.04.017>, 2015 (in Chinese).

695 Liang, S.M., Gan, W.J., Shen, C.Z., Xiao, G.R., Liu, J., Chen, W.T., Ding, X.G., Zhou, D.M.: Three-  
 696 dimensional velocity field of present-day crustal motion of the Tibetan Plateau derived from  
 697 GPS measurements. *J. Geophys. Res. Solid Earth*, 118(10), 1-11,  
 698 <https://doi.org/10.1002/2013JB010503>, 2013.

699 Liang, L.J. and Jiang, H.C.: Geochemical composition of the last deglacial lacustrine sediments in

- East Tibet and implications for provenance, weathering and earthquake events. *Quat. Inter.*, 430, 41-51, <https://doi.org/10.1016/j.quaint.2015.07.037>, 2017.
- Liu, M.: Research on the risk stone under wind loading with wind tunnel test in the Min River Valley. Chengdu University of Technology, Sichuan, p. 10-38, 2014 (in Chinese).
- Lin, M.B.: The huge Wenchuan earthquake and Longmen tectonic belt. *J. Chengdu Univ. Technol.*, 35(4), 366-370, <https://doi.org/10.3969/j.issn.1671-9727.2008.04.004>, 2008 (in Chinese).
- Liu, W.M., Yang, S.L., Fang, X.M.: Loess recorded climatic change during the last glaciation on the eastern Tibetan Plateau, western Sichuan. *J. Jilin Univ. Earth Sci. Edi.*, 43(3), 974-982, <https://doi.org/http://ir.itpcas.ac.cn/handle/131C11/2852>, 2013 (in Chinese).
- Liu, X.X., Wu, Y.Q., Jiang, Z.S., Zhan, W., Li, Q., Wen, W.X., Zhou, Z.Y.: Preseismic deformation in the seismogenic zone of the Lushan Ms 7.0 earthquake detected by GPS observations. *Sci. China, Earth Sci.*, 45(9), 1198-1207, <https://doi.org/10.1007/s11430-015-5128-0>, 2015.
- Lu, H.Y., An, Z.S.: Comparison of grain-size distribution of Red Clay and Loess-paleosol deposits in Chinese Loess Plateau. *Acta Sediment. Sinica*, 17(2), 226-232, <https://doi.org/10.3969/j.issn.1000-0550.1999.02.011>, 1999.
- Ma, K.M., Fu, B.J., Liu, S.L., Guan, W.B., Liu, G.H., Lu, Y.H., Anand, M.: Multiple-scale soil moisture distribution and its implications to ecosystem restoration in an arid river valley, China. *Land Degrad. Develop.*, 15(1), 75-85, <https://doi.org/10.1002/ldr.584>, 2004.
- Ma, Y.W., Wang, G.Z., Hu, X.W.: Tectonic deformation of Pengguan complex as a nappe. *Acta Geol. Sichuan*, 2, 110-114, 1996 (in Chinese).
- Matmon, A., Bierman, P.R., Larsen, J., Southworth, S., Pavich, M., Caffee, M.: Temporally and spatially uniform rates of erosion in the southern Appalachian Great Smoky Mountains. *Geology*, 31, 155-158, [https://doi.org/10.1130/0091-7613\(2003\)0312.0.CO;2](https://doi.org/10.1130/0091-7613(2003)0312.0.CO;2), 2003a.
- Matmon, A., Bierman, P.R., Larsen, J., Southworth, S., Pavich, M., Finkel, R., Caffee, M.: Erosion of an ancient mountain range, the Great Smoky Mountains, North Carolina and Tennessee. *Amer. J. Sci.*, 303, 817-855, <https://doi.org/10.2475/ajs.303.9.817>, 2003b.
- McKinney, G.M., Sanders, J.E.: Principles of sedimentology. Wiley, New York, No. of pages 792, 1978.
- Merritts, D., Vincent, K.R.: Geomorphic response of coastal streams to low, intermediate, and high rates of uplift, Medocino triple junction region, northern California. *GSA Bull.*, 101, 1373-

1388, [https://doi.org/10.1130/0016-7606\(1989\)101<1373:GROCST>2.3.CO;2](https://doi.org/10.1130/0016-7606(1989)101<1373:GROCST>2.3.CO;2), 1989.

Middleton, G.V.: Hydraulic interpretation of sand size distributions. *J. Geol.*, 84(4), 405-426, <https://doi.org/10.1086/628208>, 1976.

Molnar, P., Anderson, R.S., Anderson, S.P.: Tectonics, fracturing of rock, and erosion. *J. Geophys. Res. Earth Surface*, 112, F03014, <https://doi.org/10.1029/2005JF000433>, 2007.

Montgomery, D.R., Brandon, M. T.: Topographic controls on erosion rates in tectonically active mountain ranges. *Earth Planet. Sci. Lett.*, 201(3), 481-489, [https://doi.org/10.1016/S0012-821X\(0200725-2](https://doi.org/10.1016/S0012-821X(0200725-2), 2002.

Najman, Y.: The detrital record of orogenesis: A review of approaches and techniques used in the Himalayan sedimentary basins. *Earth Sci. Rev.*, 74(1-2), 1-72, <https://doi.org/10.1016/j.earscirev.2005.04.004>, 2006.

Nichols, K.K., Bierman, P.R., Caffee, M., Finkel, R., Larsen, J.: Cosmogenically enabled sediment budgeting. *Geology*, 33(2), 133-136, <https://doi.org/10.1130/g21006.1>, 2005.

Olen, S.M., Bookhagen, B., Strecker, M.R.: Role of climate and vegetation density in modulating denudation rates in the Himalaya. *Earth Planet. Sci. Lett.*, 445, 57-67, <https://doi.org/10.1016/j.epsl.2016.03.047>, 2016.

Owen, L.A.: Tectonic geomorphology: a perspective. In: Shroder, J. (Editor in Chief), Owen, L.A. (Ed.), *Treatise on Geomorphology*. Academic Press, San Diego, CA, vol. 5, *Tectonic Geomorphology*, pp. 3-12, 2013.

Passega, R.: Texture as characteristic of clastic deposition. *Bull. Amer. Assoc. Petrol. Geol.*, 41, 1952-1984, <https://doi.org/10.1306/0BDA594E-16BD-11D7-8645000102C1865D>, 1957.

Paterson, G.A., Heslop, D.: New methods for unmixing sediment grain size data. *Geochem. Geophys. Geosyst.*, 16(12), 4494-4506, <https://doi.org/info:doi/10.1002/2015GC006070>, 2015.

Perg, L.A., Anderson, R.S., Finkel, R.C.: Use of cosmogenic radionuclides as a sediment tracer in the Santa Cruz littoral cell, California, USA. *Geology*, 31, 299-302, [https://doi.org/10.1130/0091-7613\(2003\)031<0299:UOCRAA>2.0.CO;2](https://doi.org/10.1130/0091-7613(2003)031<0299:UOCRAA>2.0.CO;2), 2003.

Ren, J.J., Xu, X.W., Zhang, S.M., Yeats, R. S., Chen, J.W., Zhu, A.L., Liu, S.: Surface rupture of the 1933 Ms 7.5 Diexi earthquake in eastern Tibet: implications for seismogenic tectonics. *Geophys. J. Inter.*, 212(3), 627-1644, <https://doi.org/10.1093/gji/ggx498>, 2018.

- Riebe, C.S., Kirchner, J.W., Granger, D.E., Finkel, R.C.: Erosional equilibrium and disequilibrium in the Sierra Nevada, inferred from cosmogenic  $^{26}\text{Al}$  and  $^{10}\text{Be}$  in alluvial sediment. *Geology*, 28, 803-806, [https://doi.org/10.1130/0091-7613\(2000\)282.0.CO;2](https://doi.org/10.1130/0091-7613(2000)282.0.CO;2), 2000.
- Riebe, S.R., Kirchner, J.W., Granger, D.E., Finkel, R.C.: Strong tectonic and weak climatic control of long-term chemical weathering rates. *Geology*, 29, 511-514, [https://doi.org/10.1130/0091-7613\(2001\)0292.0.CO;2](https://doi.org/10.1130/0091-7613(2001)0292.0.CO;2), 2001.
- Sahu, B. K.: Depositional mechanisms from the size analysis of clastic sediments. *J. Sediment. Res.*, 34, 73-83, <https://doi.org/10.1306/74D70FCE-2B21-11D7-8648000102C1865D>, 1964.
- Schoenbohm, L.M., Whipple, K.X., Burchfiel, B.C., Chen, L.: Geomorphic constraints on surface uplift, exhumation, and plateau growth in the Red River region, Yunnan Province, China. *GAS Bull.*, 116, 895-909, <https://doi.org/10.1130/B25364.1>, 2004.
- Schumm, S.A., Khan, H.R.: Experimental study of channel patterns. *Nature*, 233(5319), 407-9, <https://doi.org/10.1038/233407a0>, 1971.
- Schumm, S.A., Khan, H.R.: Experimental study of channel patterns. *GAS Bull.*, 83(6), 1755-1770, [https://doi.org/10.1130/0016-7606\(1972\)83\[1755:ESOCP\]2.0.CO;2](https://doi.org/10.1130/0016-7606(1972)83[1755:ESOCP]2.0.CO;2), 1972.
- Selby, M.J.: A rock mass strength classification for geomorphic purposes, with tests from Antarctica and New Zealand: *Zeitschrift für Geomorphologie*, v. 24, p. 31–51, 1980.
- Shen, Y.Q., Guo, C.B., Wu, R.A., Ren, S.S., Su, F.R., Zhang, T.: Analysis on the development characteristics and engineering geomechanical properties of the Songpan loess, western Sichuan province, China. *J. Geomech.*, 23(5), 131-142, <https://doi.org/10.3969/j.issn.1006-6616.2017.05.013>, 2017 (in Chinese).
- Shi, W., Jiang, H.C., Mao, X., Xu, H.Y.: Pollen record of climate change during the last deglaciation from the eastern Tibetan Plateau. *PLOS ONE*, 15(5), e0232803, <https://doi.org/10.1371/journal.pone.0232803>, 2020.
- Shi, W., Jiang, H.C., Alsop, G.I., Wu, G.: A Continuous 13.3-Ka paleoseismic record constrains major earthquake recurrence in the Longmen Shan collision zone. *Front. Earth Sci.*, 10:838299, <https://doi.org/10.3389/feart.2022.838299>, 2022.
- Singh, M., Singh, I.B., Müller, G.: Sediment characteristics and transportation dynamics of the Ganga River. *Geomorphology*, 86(1/2), 144-175, <https://doi.org/10.1016/j.geomorph.2006.08.011>, 2007.

- Snyder, N., Whipple, K., Tucker, G., Merritts, D.: Landscape response to tectonic forcing: digital elevation model analysis of stream profiles in the Mendocino triple junction region, northern California. *GAS Bull.*, 112, 1250-1263, [https://doi.org/10.1130/0016-7606\(2000\)112<1250:LRTTFD>2.0.CO;2](https://doi.org/10.1130/0016-7606(2000)112<1250:LRTTFD>2.0.CO;2), 2000.
- Snyder, N.P. and Whipple, K.X.: Importance of a stochastic distribution of floods and erosion thresholds in the bedrock river incision problem. *J. Geophys. Res. Solid Earth*, 108, 2117, <https://doi.org/10.1029/2001JB001655>, 2003.
- Stock, J. D., Dietrich, W. E.: Valley incision by debris flows: evidence of a topographic signature. *Water Resour. Res.*, 39(4), ESG 1-1, <https://doi.org/10.1029/2001WR001057>, 2003.
- Stokes, M., Mather, A.E., Belfoul, A., Farik, F.: Active and passive tectonic controls for transverse drainage and river gorge development in a collisional mountain belt (Dades Gorges, High Atlas Mountains, Morocco). *Geomorphology*, 102(1), 2-20, <https://doi.org/10.1016/j.geomorph.2007.06.015>, 2008.
- Stokes, M., Mather, A.E., Harvey, A.M.: Quantification of river-capture-induced base-level changes and landscape development, Sorbas Basin, SE Spain. *Geol. Soc. London Spec. Publ.*, 191(1), 23-35, <https://doi.org/10.1144/GSL.SP.2002.191.01.03>, 2002.
- Sun, D.H., Bloemendal, J., Rea, D.K., An, Z.S., Vandenberghe, J., Lu, H.Y., Sun, R.X., Liu, T.S.: Bimodal grain-size distribution of Chinese loess, and its palaeoclimatic implications. *Catena*, 55(3), 325-340, [https://doi.org/10.1016/S0341-8162\(03\)00109-7](https://doi.org/10.1016/S0341-8162(03)00109-7), 2004.
- Sun, D.H., Bloemendal, J., Rea, D.K., Vandenberghe, J., Jiang, F.C., An, Z.S., Su, R.X.: Grain-size distribution function of polymodal sediments in hydraulic and aeolian environments, and numerical partitioning of the sedimentary components. *Sediment. Geol.*, 152(3-4), 263-277, [https://doi.org/10.1016/S0037-0738\(02\)00082-9](https://doi.org/10.1016/S0037-0738(02)00082-9), 2002.
- Sun, J.M, Li, S.H., Muhs, D. R., Li, B.: Loess sedimentation in Tibet: provenance, processes, and link with Quaternary glaciations, *Quat. Sci. Rev.*, 26(17-18), 2265-2280, <https://doi.org/10.1016/j.quascirev.2007.05.003>, 2007.
- Tan, X.B., Liu, Y.D., Lee, Y.H., Lu, R.Q., Xu, X.W., Suppe, J., Shi, F., Xu, C.: Parallelism between the maximum exhumation belt and the Moho ramp along the eastern Tibetan Plateau margin: Coincidence or consequence?. *Earth Planet. Sci. Lett.*, 507, 73-84,

818 <https://doi.org/10.1016/j.epsl.2018.12.001>, 2019.

819 Tsoar, H., Pye, K.: Dust transport and the question of desert loess formation. *Sedimentology*, 34(1),  
820 139-153, <https://doi.org/10.1111/j.1365-3091.1987.tb00566.x>, 1987.

821 Vandenberghe, J.: Grain size of fine-grained windblown sediment: a powerful proxy for process  
822 identification. *Earth Sci. Rev.*, 121, 18-30, <https://doi.org/10.1016/j.earscirev.2013.03.001>,  
823 2013.

824 Wang, J., Jin, Z.D., Hilton, R.G., Zhang, F., Densmore, A.L., Li, G., West A.J.: Controls on fluvial  
825 evacuation of sediment from earthquake-triggered landslides. *Geology*, 43(2), 115-118,  
826 <https://doi.org/10.1130/G36157.1>, 2015.

827 Wang, P., Zhang, B., Qiu, W.L., Wang, J.C.: Soft-sediment deformation structures from the Diexi  
828 paleo-dammed lakes in the upper reaches of the Minjiang River, east Tibet. *J. Asian Earth Sci.*,  
829 40(4), 865-872, <https://doi.org/10.1016/j.jseaes.2010.04.006>, 2011.

830 Wang, P., Scherler, D., Liu-Zeng, J., Mey, J., Avouac, J.P., Zhang, Y., Shi, D.: Tectonic control of  
831 Yarlung Tsangpo gorge revealed by a buried canyon in southern Tibet. *Science*, 346, 978-981,  
832 <https://doi.org/10.1126/science.1259041>, 2014.

833 Wang, W., Godard, V., Liu-Zeng, J., Scherler, D., Xu, C., Zhang, J.Y., Xie, K.J., Bellier, O.,  
834 Ansberque, C., Sigoyer, J., Team, A.: Perturbation of fluvial sediment fluxes following the  
835 2008 Wenchuan earthquake. *Earth Surf. Process Land.*, 42(15), 2611-2622,  
836 <https://doi.org/10.1002/esp.4210>, 2017.

837 Wang, W., Godard, V., Liu-Zeng, J., Zhang, J.Y., Li, Z.G., Xu, S., Yao, W.Q., Yuan, Z.D., Aumaître,  
838 G., Bourlès, D.L., Keddadouche, K.: Tectonic controls on surface erosion rates in the Longmen  
839 Shan, eastern Tibet. *Tectonics*, 40(3), <https://doi.org/10.1029/2020TC006445>, 2021.

840 Wang, X.G., Li, C.Y., Lu, L.X., Dong, J.B.: Analysis of the late Quaternary activity along the  
841 Wenchuan-Maoxian fault-middle of the back- range fault at the Longmen Shan fault zone.  
842 *Seism. Geol.*, 39(3), 572-586, <https://doi.org/10.3969/j.issn.0253-4967.2017.03.010>, 2017.

843 Weltje, G.L.: End-member modeling of compositional data: Numerical-statistical algorithms for  
844 solving the explicit mixing problem. *Mathemat. Geol.*, 29(4), 503-549,  
845 <https://doi.org/10.1007/BF02775085>, 1997.

846 Wei, X.T., Jiang, H.C., Xu, H.Y., Fan, J.W., Shi, W., Guo, Q.Q., Zhang, S.Q.: Response of

sedimentary and pollen records to the 1933 Diexi earthquake on the eastern Tibetan Plateau. *Ecol. Indicators*, 129, 107887, <https://doi.org/10.1016/j.ecolind.2021.107887>, 2021.

Whipple, K.X.: Bedrock rivers and the geomorphology of active orogens. *Ann. Rev. Earth Planet. Sci.*, 32, 151-185, <https://doi.org/10.1146/annurev.earth.32.101802.120356>, 2004.

Whittaker, A.C., Attalw, M., Allenn, P.A.: Characterising the origin, nature and fate of sediment exported from catchments perturbed by active tectonics. *Basin Res.*, 22, 809-828, <https://doi.org/10.1111/j.1365-2117.2009.00447.x>, 2010.

Whittaker, A. C., Cowie, P.A., Attal, M., Tucker, G. E., Roberts, G.P.: Contrasting transient and steady-state rivers crossing active normal faults: new field observations from the central Apennines, Italy. *Basin Res.*, 19(4), 529-556, <https://doi.org/10.1111/j.1365-2117.2007.00337>, 2007.

Wu, H.B., Liu, X.M., Lv, B., Ma, M.M., Ji, J.P., Wang, W.Y., Zhang, Y.Y., Hou, J.L.: Aeolian origin of the Twelve Apostles section, in Australia. *Quat. Sci.*, 37(1), 82-96, <https://doi.org/10.11928/j.issn.1001-7410.2017.01.08>, 2017 (in Chinese).

Wobus, C., Heimsath, A., Whipple, K. Hodges, K.: Active out-of-sequence thrust faulting in the central Nepalese Himalaya. *Nature*, 434, 1008-1011, <https://doi.org/10.1038/nature03499>, 2005.

Wobus, C.W., Tucker, G.E., and Anderson, R.S.: Does climate change create distinctive patterns of landscape incision? *J. Geophys. Res.*, 115, F04008, <https://doi.org/10.1029/2009JF001562>, 2010.

Xu, C., Xu, X.W., Dai, F.C., Xiao, J.Z., Tan, X.B., Yuan, R.M.: Landslides hazard mapping using GIS and weight of evidence model in Qingshui River watershed of 2008 Wenchuan earthquake struck region. *J. Earth Sci.*, 23(1), 97-120, <https://doi.org/10.1007/s12583-012-0236-7>, 2012.

Xu, C., Xu, X.W., Yao, X., Dai, F.C.: Three, nearly complete inventories of landslides triggered by the May 12, 2008 Wenchuan Mw 7.9 earthquake of China and their spatial distribution statistical analysis. *Landslides*, 11(3), 441-461, <https://doi.org/10.1007/s10346-013-0404-6>, 2014.

Xu, H.Y., Jiang, H.C., Liu, K., Zhong, N.: Potential pollen evidence for the 1933 M7.5 Diexi earthquake and implications for post-seismic landscape recovery. *Enviro. Res. Lett.*, 15:094043,

<https://doi.org/10.1088/1748-9326/ab9af6>, 2020.

Xu, H.Y., Jiang, H.C., Yu, S., Yang, H.L., Chen, J.: OSL and pollen concentrate <sup>14</sup>C dating of dammed lake sediments at Maoxian, east Tibet, and implications for two historical earthquakes in AD 638 and 952. *Quat. Inter.*, 371, 290-299, <https://doi.org/10.1016/j.quaint.2014.09.045>, 2015.

Zhang, F., Jin, Z.D., West, A.J., An, Z.S., Hilton, R.G., Wang, J., Li, G., Densmore, A.L., Yu, J.M., Qiang, X.K., Sun, Y.B., Li, L.B., Gou, L.F., Xu, Y., Xu, X.W., Liu, X.X., Pan, Y.H., You, C.F.: Monsoonal control on a delayed response of sedimentation to the 2008 Wenchuan earthquake. *Sci. Adv.*, 5(6), eaav7110, <https://doi.org/10.1126/sciadv.aav7110>, 2019.

Zhang, P.Z., Deng, Q.D., Zhang, M.G., Ma, J., Gan, W.J., Wei, M., Mao, F.Y., Wang, Q.: Active tectonic blocks and strong earthquakes in the continent of China. *Sci. China*, 46, 13-24, <https://doi.org/10.3969/j.issn.1674-7313.2003.z2.002>, 2003.

Zhang, P.Z., Zhou, Z.Y., Xu, C.H., Zhang, Q.L.: Geochemistry of Pengguan complex in the Longmenshan region, western Sichuan Province, SW China: petrogenesis and tectonic implications. *Geotecton. Metallog.*, 32(1), 105-116, <https://doi.org/10.3969/j.issn.1001-1552.2008.01.014>, 2008 (in Chinese).

Zhang, S.Q., Jiang, H.C., Fan, J.W., Xu, H.Y., Shi, W., Guo, Q.Q. and Wei, X.T.: Accumulation of a last deglacial gravel layer at Diexi, eastern Tibetan Plateau and its possible seismic significance. *Front. Earth Sci.*, 9:797732, <https://doi.org/10.3389/feart.2021.797732>, 2021.

Zhang, Y.Q., Yang, N., Meng, H.: Deep-incised valleys along the Minjiang river upstream and their responses to the uplift of the West Sichuan Plateau, China. *J. Chengdu Univ. Technol.*, 32(4), 331-339, <https://doi.org/10.3969/j.issn.1671-9727.2005.04.001>, 2005 (in Chinese).

Zhou R.J., Li, Y., Densmore, A.L., Ellis, M.A., He, Y.L., Wang, F.L., Li, X.G.: Active tectonics of the eastern margin of the Tibet Plateau. *J. Mineral. Petrol.*, 26(2),40-51, <https://doi.org/10.3969/j.issn.1001-6872.2006.02.007>, 2006 (in Chinese).

Zhou, R.J., Pu, X.H., He, Y.L., Li, X.G., Ge, T.Y.: Recent activity of Minjiang fault zone, uplift of Minshan Block and their relationship with seismicity of Sichuan. *Seism. Geol.*, 22(3),285-294, <https://doi.org/CNKI:SUN:DZDZ.0.2000-03-009>, 2000 (in Chinese).

Zhou, R.Y., Wen, X.Y., Lu, L., Li, Y.X., Huang, C.M.: Holocene paleosols and paleoclimate for the



905 arid upper Minjiang River valley in the eastern Tibetan Plateau. *Catena*, 206, 105555,  
 906 <https://doi.org/10.1016/j.catena.2021.105555>, 2021.

907 Zhong, N., Jiang, H.C., Li, H.B., Xu, H.Y., Shi, W., Zhang, S.Q., Wei, X.T.: Last Deglacial Soft-  
 908 Sediment Deformation at Shawan on the Eastern Tibetan Plateau and Implications for  
 909 Deformation Processes and Seismic Magnitudes. *Acta Geol. Sinica*, 93(2), 430-450,  
 910 <https://doi.org/10.1111/1755-6724.13773>, 2019.

911 Zhong, N., Song, X.S., Xu, H.Y., Jiang, H.C.: Influence of a tectonically active mountain belt on its  
 912 foreland basin: Evidence from detrital zircon dating of bedrocks and sediments from the eastern  
 913 Tibetan Plateau and Sichuan Basin, SW China. *J. Asian Earth Sci.*, 146, 251-264,  
 914 <https://doi.org/10.1016/j.jseaes.2017.05.035>, 2017.

915 Zondervan, J., Stokes, M., Boulton, S., Telfer, M., Mather, A.: Rock strength and structural controls  
 916 on fluvial erodibility: Implications for drainage divide mobility in a collisional mountain belt.  
 917 *Earth Planet. Sci. Lett.*, 538, 116221, <https://doi.org/10.1016/j.epsl.2020.116221>, 2020.